Dalton Transactions

Improved Solubility of Titanium-Doped Polyoxovanadate Charge Carriers for Symmetric Non-aqueous Redox Flow Batteries

Journal:	*Dalton Transactions*
Manuscript ID	DT-ART-10-2023-003642.R1
Article Type:	Paper
Date Submitted by the Author:	22-Nov-2023
Complete List of Authors:	Dagar, Mamta; University of Rochester, Chemistry Dissanyake, D. M. M. Mevan; University of Rochester, Chemistry Kessler, Daniel; University of Rochester, Chemistry Corr, Molly; University of Rochester, Chemistry McPherson, Joshua; University of Rochester, Chemistry Brennessel, William; University of Rochester, Department of Chemistry McKone, James; University of Pittsburgh, Chemical and Petroleum Engineering Matson, Ellen; University of Rochester, Chemistry

ARTICLE

Improved Solubility of Titanium-Doped Polyoxovanadate Charge Carriers for Symmetric Non-aqueous Redox Flow Batteries

Received 00th January 20xx,
Accepted 00th January 20xx

DOI: 10.1039/x0xx00000x

Mamta Dagar,[a] D. M. M. Mevan Dissanyake,[a] Daniel N. Kesler,[a] Molly Corr,[a] Joshua D. McPherson,[a] William W. Brennessel,[a] James R. McKone[b] and Ellen M. Matson*[a]

Non-aqueous redox flow batteries constitute a promising solution for grid-scale energy storage due to the ability to achieve larger cell voltages than can be readily accessed in water. However, their widespread application is limited by low solubility of the electroactive species in organic solvents. In this work, we demonstrate that organic functionalization of titanium-substituted polyoxovanadate-alkoxide clusters increases the solubility of these assemblies over that of their homoleptic congeners by a factor of >10 in acetonitrile. Cyclic voltammetry, chronoamperometry, and charge–discharge cycling experiments are reported, assessing the electrochemical properties of these clusters relevant to their ability to serve as multielectron charge carriers for energy storage. The kinetic implications of ligand variation are assessed, demonstrating the role of ligand structure on the diffusivity and heterogeneous rates of electron transfer in mixed-metal charge carriers . Our results offer new insights into the impact of structural modifications on the physicochemical properties of these assemblies.

Introduction

Redox flow batteries (RFBs) are electrochemical energy storage devices that interconvert chemical and electrical energy using soluble redox active species.[1] They can be classified as aqueous or non-aqueous depending upon the solvent composition. To date, the most advanced flow battery technologies leverage soluble redox couples in acidic, aqueous solutions.[2] However, non-aqueous RFBs (NAqRFBs) remain an intriguing alternative, as the use of organic solvents offers a wide range of working temperatures, and potentially higher energy densities due to the improved electrochemical stability window of organic solvents.[3] Successful implementation of NAqRFB technologies in grid-scale energy storage is limited by lack of suitable membranes, cost and safety risks associated with organic solvents, and low solubilities of many redox-active species in polar organic solvents like acetonitrile. Additional challenges for NAqRFBs manifest as poor round-trip voltage efficiencies owing to three major losses that result in the form of overpotentials required for charge-discharge reactions – transport, resistive, and kinetic losses.[4] For instance, the use of organic solvents as electrolytes can result in higher ionic resistances as compared to aqueous solutions. These transport losses can impact the overall efficiency and performance of NAqRFBs and may be more pronounced as compared to their aqueous counterparts.[5] Accordingly, charge carriers must be designed to exhibit (1) high solubility in organic solvent(s); (2) kinetically facile and reversible redox reactions; (3) a large potential window between the desired redox events; and (4) high chemical and electrochemical stability across the required oxidation states.

A popular method for the development of efficient charge carriers for applications in NAqRFBs is designing metal-based coordination complexes that exhibit at least two redox events exhibiting large (>>1 V) differences in standard reduction potential. Such systems allow for symmetric flow battery design, wherein the posolyte and negolyte are comprised of the same material, preventing cross-contamination of the active species due to membrane crossover.[6, 7] One particularly intriguing class of redox-active inorganic compounds for this application are polyoxometalates (POMs). These metal oxide clusters are electrochemically robust, and display multiple redox events spread across a wide range of potentials,[8] which makes them excellent candidates for symmetric cell design.[9-13] However, their limited solubility in organic solvent(s) is a major challenge to obtain functional RFB systems due to the fact that important battery metrics, including energy conversion efficiency, volumetric energy density, and capacity, depend fundamentally on this property.[14, 15]

One strategy for improving the solubility of POMs in organic solvent invokes incorporation of organic moieties at the metal oxide surface.[16-19] In recent years, there has been increased attention paid to the synthesis of POM-based organic-inorganic hybrids, which are generated via covalent grafting of organic functional groups to the surface of the POM framework.[20, 21] This technique is advantageous as it allows the attachment of specific functional groups in a predictable and reliable manner. The formation of organofunctionalized, polyoxovanadates, henceforth referred to as polyoxovanadate-alkoxide (POV-alkoxide) clusters, is a particularly popular area of research, due

[a] Department of Chemistry, University of Rochester, Rochester NY 14627, USA.
[b] Department of Chemical and Petroleum Engineering, University of Pittsburgh, Pittsburgh PA 15261, USA.

Electronic Supplementary Information (ESI) available: Experimental procedures, spectroscopic and analytical data, crystallographic parameters, and X-ray crystal structure of $Ti_2V_4TRIOL^B$. For ESI and crystallographic data in CIF or other electronic format see DOI: 10.1039/x0xx00000x

to the increased basicity of bridging oxide positions at the surface of the cluster.[22-24] Zubieta and coworkers exemplified this approach through the isolation of a wide array of hexavanadium systems featuring trisalkoxy-μ-bridging groups (TRIOL^R).[25-27] These TRIOL^R ligands are well established in the literature owing to their compatibility with a wide variety of functional groups, which allows to tune the physicochemical properties of the resultant cluster.[26, 28-30]

In the context of the development of charge carriers for NAqRFBs, our group has reported the installation of TRIOL moieties at the surface of low-valent POV-alkoxide clusters (**Figure 1**).[31-33] These synthetic modifications increase the solubility by an order of magnitude in comparison to the homoleptic congener. In this work, we report the functionalization of the surface of titanium-substituted POV-alkoxide clusters with the same solubility-enhancing TRIOL ligands. Interest in these synthetic targets results from prior work from our laboratory, establishing that incorporation of titanium ions within the Lindqvist core results in widening of the redox window of the charge carrier by ~1 V. However, the poor solubility of the methoxide-substituted derivative of the heterometallic assembly (< 0.05 M) motivates additional structural modifications to increase the energy density of this system.[34] Our results summarize the synthesis of two new TRIOL-substituted TiPOV-alkoxide clusters, as well as their solubilities and performance as charge carriers in NAqRFBs. This synthetic modification improves the solubility of these clusters by an order of magnitude. Collectively, the understanding gained from these investigations informs strategies for improved energy densities in NAqRFBs.

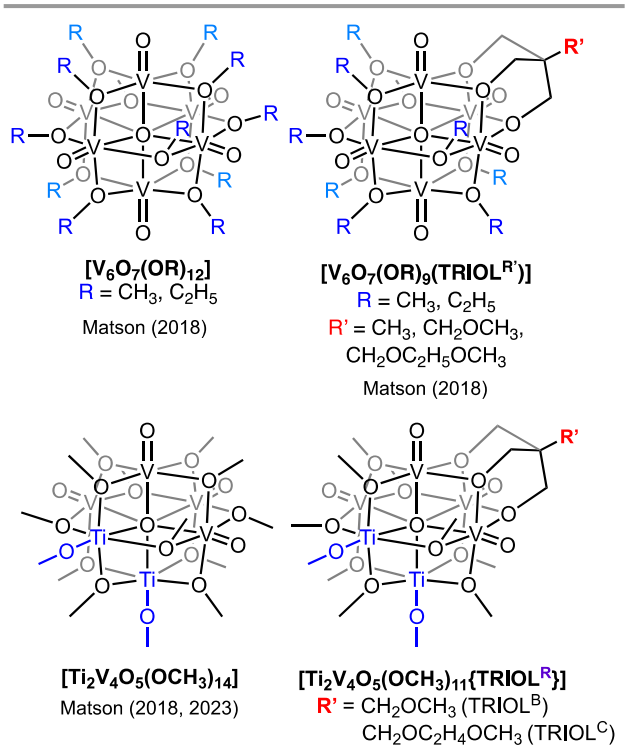

Figure 1. Overview of the use of tridentate ligands to enhance the solubility, and thus theoretical energy density, of POV-alkoxide clusters as charge carriers for NAqRFBs.

Experimental

General considerations. Unless otherwise noted, all manipulations were carried out in the absence of water and oxygen in a UniLab MBraun inert atmosphere glovebox under a dinitrogen atmosphere. The glassware was oven dried for a minimum of 4 hours and cooled in an evacuated antechamber prior to use in the drybox. Anhydrous methanol was purchased from Sigma-Aldrich and stored over activated 4 Å molecular sieves purchased from Fisher Scientific. All other solvents were dried and deoxygenated on a Glass Contour System (Pure Process Technology, LLC) and stored over activated 3 Å molecular sieves purchased from Fisher Scientific. Ti(O^iPr)$_4$ was purchased from Sigma Aldrich and used as received. Tetrabutylammonium hexafluorophosphate ([^{n}Bu$_4$N][PF$_6$]) was purchased from Sigma-Aldrich. [^{n}Bu$_4$N][PF$_6$] was recrystallized thrice using hot methanol, and stored under dynamic vacuum for a minimum of two days prior to use. VO(OCH$_3$)$_3$,[35] [Ti$_2$V$_4$O$_5$(OCH$_3$)$_{14}$],[36] CH$_3$C(CH$_2$O)$_3$CCH$_2$OCH$_3$,[37] and CH$_3$C(CH$_2$O)$_3$CCH$_2$OC$_2$H$_4$OCH$_3$[37] were synthesized according to previously reported methods.

^{1}H NMR spectra were recorded at 500 MHz on Bruker DPX-500 spectrometer locked on the signal of deuterated solvents. All chemical shifts were reported relative to the peak of residual ^{1}H signal in deuterated solvents.[38] CD$_3$CN and CDCl$_3$ were purchased from Cambridge Isotope Laboratories and used as received. Electronic absorption measurements were recorded at room temperature in acetonitrile (MeCN) in a sealed 1 cm quartz cuvette with an Agilent Cary 60 UV/Vis spectrophotometer. Infrared spectra were recorded on a Shimadzu IRAffinity-1 Fourier Transform Infrared spectrophotometer and are reported in wavenumbers (cm^{-1}).

Modified Procedure for the preparation of Protected Ligand Precursor (**PLP**). The synthesis of PLP has been modified from prior reports.[39 31] The preparation of PLP was conducted outside of the glovebox. A 1000 mL round-bottomed flask was charged with ground pentaerythritol (50 g, 367 mmol) and p-toluenesulfonic acid monohydrate (0.9 g, 5.2 mmol) and a stir bar. The flask was placed under an atmosphere of argon and equipped with a reflux condenser. Subsequently, toluene (500 mL) was added. The reaction was refluxed for 1 h, after which triethyl orthoacetate (75 mL, 409 mmol) was added. The resulting suspension was refluxed until the solution turned clear, with no solid residue visible (~48 h). 1.1 mL of triethyl amine was added to the flask, and the solution was filtered while hot. The solution was concentrated under reduced pressure to obtain PLP as a white crystalline solid. Characterization of the obtained product was performed via ^{1}H NMR spectroscopy and matched with the reported spectrum (Supporting Information, Figure S1).

Synthesis of [Ti$_2$V$_4$O$_5$(OCH$_3$)$_{11}$(OCH$_2$)$_3$CCH$_2$OCH$_3$] (**Ti$_2$V$_4$TRIOL^B**). VO(OCH$_3$)$_3$ (0.25 g, 1.56 mmol), titanium isopropoxide (0.22 g,

0.78 mmol), and PL[b] (0.14 g, 0.78 mmol) were combined in the Teflon liner of a 50 mL stainless steel autoclave reactor and dissolved in methanol (25 mL) The reactor was sealed and heated to 150 °C for 48 h. Initial workup of the cluster was performed outside of the glovebox under ambient conditions. After cooling the reaction vessel to room temperature, the crude mixture was passed through a syringe filter to remove any solid remains and the volatiles were removed under reduced pressure. The dark brown residue was dried under reduced pressure on the Schlenk line for 4 hours and transferred back to the glovebox for further purification. The product was extracted with diethyl ether (3 × 10 mL) and filtered over silica to recover a brown filtrate. Volatiles were again removed under vacuum inside the glovebox to yield a dark brown oil. The obtained oil was again dissolved in diethyl ether (~ 20 mL) and the contents were filtered over silica inside the glovebox. The resulting product was dried under reduced pressure to yield **Ti_2V_4TRIOL[B]** as a dark brown oil. Yield: 0.14 g, 0.16 mmol, 21 %. FT-IR (ATR, cm^{-1}): 1125 (O_t-CH_3), 1017 (O_b-CH_3), 976 (V=O). UV-Vis (CH_3CN, 21 °C) λ = 418 nm (ε = 656 $M^{-1}cm^{-1}$), 1000 nm (ε = 121 $M^{-1}cm^{-1}$). Elemental analysis for $C_{17}H_{44}O_{20}Ti_2V_4 \bullet ¼\ C_6H_{14}$ (M_W = 889.56 g mol^{-1}): Calc. C, 24.98; H, 5.38; N, 0.00. Found, C, 25.03; H, 5.07; N: 0.08.

Synthesis of $[Ti_2V_4O_5(OCH_3)_{11}(OCH_2)_3CCH_2OC_2H_4OCH_3]$ (**Ti_2V_4TRIOL[C]**). $VO(OCH_3)_3$ (0.25 g, 1.56 mmol), titanium isopropoxide (0.22 g, 0.78 mmol), and PL[c] (0.18 g, 0.78 mmol) were combined in the Teflon liner of a 50 mL stainless steel autoclave reactor and dissolved in methanol (25 mL). The reactor was sealed and heated to 150 °C for 48 h. Initial workup of the cluster was performed outside of the glovebox under ambient conditions. After cooling the reaction vessel to room temperature, the crude mixture was passed through a syringe filter to remove any solid remains and the volatiles were removed under reduced pressure. The dark brown residue was dried over the Schlenk line for 4 hours and transferred back to the glovebox for further purification. The product was extracted with diethyl ether (3 × 10 mL) and filtered over silica. Volatiles were again removed under vacuum inside the glovebox to yield a dark brown oil. The obtained oil was dissolved in diethyl ether (~ 20 mL) and the contents were filtered over silica inside the glovebox. The resulting product was dried under reduced pressure to yield **Ti_2V_4TRIOL[C]** as a dark brown oil. Yield: 0.17 g, 0.19 mmol, 26 %. FT-IR (ATR, cm^{-1}): 1125 (O_t-CH_3), 1018 (O-CH_3), 972 (V=O). UV-Vis (CH_3CN, 21 °C) λ = 392 nm (ε = 877 $M^{-1}cm^{-1}$), 1000 nm (ε = 122 $M^{-1}cm^{-1}$). Elemental analysis for $C_{19}H_{48}O_{21}Ti_2V_4 \bullet ¼\ C_6H_{14}$ (M_W = 933.62 g mol^{-1}): Calc., C, 26.37; H, 5.56; N, 0.00. Found, C, 26.79; H, 5.46; N, -0.027.

Cyclic voltammetry. Cyclic voltammetry (CV) was performed using a three-electrode setup inside a nitrogen filled glove box (Vigor Tech, USA) using a Bio-Logic SP 150 potentiostat/galvanostat and the EC-Lab software suite. The concentrations of **Ti_2V_4** ($[Ti_2V_4O_5(OCH_3)_{14}]$), **Ti_2V_4TRIOL[B]**, and **Ti_2V_4TRIOL[C]** were kept at 5 mM and 100 mM supporting electrolyte ($[^nBu_4N][PF_6]$) was used. CVs were recorded using a 3 mm diameter glassy carbon working electrode (CH Instruments, USA), a Pt wire auxiliary electrode (CH Instruments, USA), and a $Ag|Ag^+$ non-aqueous reference electrode with 0.01 M $AgNO_3$ in 0.1 M $[^nBu_4N][PF_6]$ in MeCN (BASi, USA). CVs were iR compensated via positive feedback at 95% with solution resistance measurements collected at 100 kHz using the ZIR tool included within the EC-Lab software. The remaining 5% of uncompensated resistance was accounted for by manual correction.[40]

Bulk electrolysis. Bulk electrolysis experiments were performed in a H-cell with a glass frit separator (Porosity = 10-16 µm, Pine Research, USA) using a Bio-Logic SP 150 potentiostat/galvanostat. An active species concentration of 5 mM was used. The working electrode compartment contained 5 mL of the active species with 0.1 M supporting electrolyte ($[^nBu_4N][PF_6]$) in MeCN and counter electrode compartment consisted of 5 mL of 0.1 M electrolyte ($[^nBu_4N][PF_6]$) in MeCN. A Pt mesh working electrode and a Pt wire counter electrode were used. Bulk electrolysis experiments were carried out using chronoamperometry techniques available in EC lab software suite at constant potentials, selected from CV experiments.

Solubility measurements. A 0.1 M concentration of $[^nBu_4N][PF_6]$ was used in all samples to simulate the electrochemical conditions of the cells studied in this work. All samples were referenced against a baseline of 0.1 M $[^nBu_4N][PF_6]$ in MeCN. To establish a calibration curve, 10 mM stock solutions were prepared by combining the supporting electrolyte (0.194 g $[^nBu_4N][PF_6]$), the appropriate TiPOV-alkoxide cluster (e.g. 0.043 g of **Ti_2V_4TRIOL[B]**; 0.046 g of **Ti_2V_4TRIOL[C]**) and 5 mL of solvent in a vial and stirring until completely dissolved. Additionally, a stock solution of 0.1 M $[^nBu_4N][PF_6]$ was prepared by combining 0.581 g $[^nBu_4N][PF_6]$, in 15 mL of MeCN. In a cuvette, 0.3 mL of the cluster stock solution was added and was subsequently diluted with 2.7 mL of the 0.1 M $[^nBu_4N][PF_6]$ stock solution. This process was repeated 4 times to obtain solutions with the following concentrations: 1.0 mM, 0.8 mM, 0.6 mM, 0.4 mM, and 0.2 mM. The electronic absorption spectra (UV-Vis) of these samples were recorded, and their absorbances at 415 nm were plotted against the sample's concentration to obtain a calibration based on the Beer-Lambert equation.

Three saturated solutions for each solvent were prepared by stirring an excess of Ti-POV in 5 mL of 0.1 M electrolyte ($[^nBu_4N][PF_6]$) solution for a minimum of 24 hours. These solutions were passed through a syringe filter (EZFlow Syringe Filter, diameter = 25 mm, pore size = 0.22 µm) to remove undissolved TiPOV-alkoxide. 10 µL aliquots of each solution were removed and diluted such that the absorbance of the sample fell between 0.1 and 1.0. The absorbance of each diluted sample at appropriate wavelength (**Ti_2V_4TRIOL[B]** = 422 nm; **Ti_2V_4TRIOL[C]** = 415 nm) was recorded, and the concentration of the diluted sample was determined using the Beer's law equation from the corresponding calibration curve. The concentration of each saturated solution was then calculated from the concentration of the diluted sample. See Supporting Information for figures and details pertaining to the solubility

calculations performed for each Ti-substituted POV-alkoxide cluster reported.

Charge-discharge experiments. Charge-discharge testing was conducted in a nitrogen filled glove box using a glass H-cell separated by a microporous glass frit (P5, 1.6 µm, Adams and Chittenden, USA) and a Bio-Logic SP 300 potentiostat/galvanostat. The electrolyte solutions used in charge-discharge experiments were 5 mM Ti-POV in 0.1 M electrolyte ($[^nBu_4N][PF_6]$) in MeCN. Each compartment of the H-cell was filled with 5 mL of electrolyte solution. Two graphite felt electrodes (1 × 1 × 0.5 cm, Fuel Cell Store, USA) were placed in the posolyte and negolyte chambers. For the symmetrically unbalanced cycling experiment, the volume of the negolyte was increased to 10 mL, whereas the posolyte was maintained at 5 mL. Electrodes were attached to Pt wire current collectors submerged in the electrolyte solutions (~0.5 cm). Graphite felt electrodes were soaked in electrolyte solutions for 24 hours before each experiment. A sequential galvanostatic–potentiostatic charge–discharge method was adopted using a charging current of 0.2 mA until the potential reached 1.9 V.[41] Subsequently, the potential was held at 1.9 V until the current dropped to 0.02 mA. Similarly, a discharging current of 0.2 mA was applied until a cut-off potential of 1.4 V was reached, followed by a potentiostatic discharge at 1.4 V until the current reached a value of 0.02 mA. For the duration of the charge-discharge experiments, both half cells were stirred at ~1,000 rpm.

For the polarity reversal experiments, purely galvanostatic mode of charge-discharge was followed. A (dis)charging current of 0.2 mA was utilized throughout. The cell was allowed to operate for 4 consecutive cycles with potential cut-offs for charging and discharging as 1.9 V and 1.4 V, respectively. Subsequently, the polarity of the electrochemical was reversed by applying the charging and discharging potential cut-offs as -1.4 V and -1.9 V, respectively. These conditions were maintained for 4 cycles, after which the conditions were reverted to the original value. Both half cells were stirred at ~1,000 rpm for the entire duration of the experiment.

Results & Discussion

Organic functionalization of $[Ti_2V_4O_5(OCH_3)_{14}]$. Our group has demonstrated that installation of a TRIOL ligand featuring ether functional groups at the surface of POV-alkoxide clusters can enhance the solubility of the assembly in MeCN.[31] In this work, we extend this finding to a Ti-doped POV-alkoxide cluster, $[Ti_2V_4O_5(OCH_3)_{14}]$ (**Ti_2V_4**), which possess large cell voltage windows ($\Delta E_{1/2}$ ~ 1.7 and 2.6 V for the inner and outer redox couples, respectively). Synthetic insights from our previously published preparation of TRIOL-functionalized di-titanium POV-alkoxides were invoked.[32]

To access the desired ether-functionalized TiPOV–alkoxide clusters, we first generated the alkoxyether-substituted pentaerythritol derivatives through a modified procedure. Briefly, protection of three hydroxyl substituents of pentaerythritol was accomplished by addition of triethylorthoacetate to generate the protected ligand precursor (PLP), $CH_3C(OCH_2)_3CCH_2OH$.[39] The remaining -OH group of PLP was functionalized according to the previously established protocols by our group to yield $CH_3C(OCH_2)_3CCH_2OCH_3$ (PL^b) and $CH_3C(OCH_2)_3CCH_2OC_2H_4OCH_3$ (PL^c).[31]

Following successful synthesis and characterization of the ligands PL^b and PL^c, we sought to generate the TRIOL-functionalized derivates of Ti-POVs. We hypothesized that the innate acidity of the solvothermal syntheses, combined with the reducing nature of methanol at elevated temperatures, would preclude the requirement of an additional ligand deprotection step. Indeed, the methoxyether substituted TRIOL-functionalized TiPOV-alkoxide cluster, $[Ti_2V_4O_5(OCH_3)_{11}(OCH_2)_3CCH_2OCH_3]$ (**$Ti_2V_4TRIOL^B$**), was produced in moderate yield via solvothermal treatment of the ligand precursor, PL^b (1 equiv), $Ti(O^iPr)_4$ (1 equiv) and $VO(OCH_3)_3$ (2 equiv) in methanol (**Scheme 1**, see Experimental Section for more details). The crude reaction mixture presents as a dark brown liquid with solid precipitate at the bottom of the autoclave. Analysis of each of the phases using cyclic voltammetry (CV) suggests that the desired product is found in the liquid phase; analysis of the filtrate reveals four reversible redox events, consistent with the electrochemical profiles previously reported for TiPOV-alkoxide clusters (Figure S2).

Scheme 1. Synthesis of **$Ti_2V_4TRIOL^B$** and **$Ti_2V_4TRIOL^C$.**

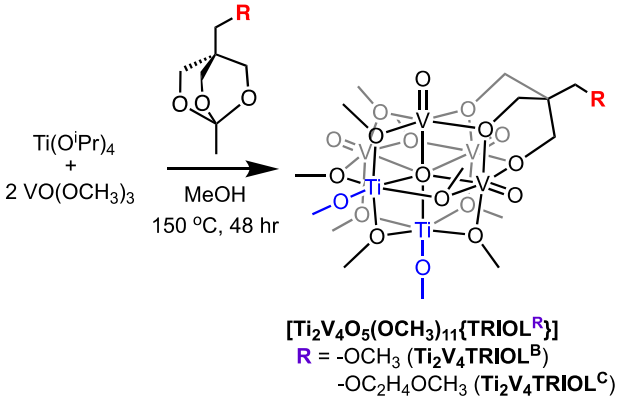

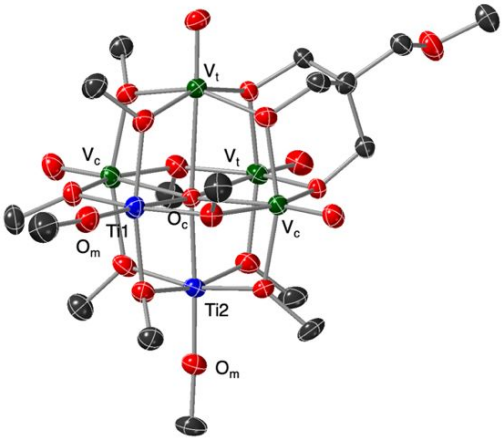

Figure 2. Molecular structure of $Ti_2V_4TRIOL^B$ shown with 40% probability ellipsoids. Hydrogen atoms and solvent molecules are removed for clarity. Key: blue ellipsoids: To; green ellipsoids: V; red ellipsoids: O; grey ellipsoids: C.

Following work-up, further characterization of the complex was performed via infrared (IR) and electronic absorption spectroscopies. In the IR spectra of **$Ti_2V_4TRIOL^B$**, two absorption features are observed at ~975 cm^{-1} and ~1020 cm^{-1}, which correspond to $\nu(V{=}O_t)$ (O_t = terminal oxo) and $\nu(O_b\text{-}CH_3)$ (O_b = bridging oxo), respectively (Figure S3). Additionally, a transition at 1125 cm^{-1} is observed, consistent with the $\nu(O_t\text{-}CH_3)$ of the terminal alkoxide ligands bound to the heterometallic titanium centres. Analysis of the electronic absorption spectrum of **$Ti_2V_4TRIOL^B$** reveals broad feature around 420 nm, assigned as an electron transfer event between $V^{IV}(d^1)$ and $Ti^{IV}(d^0)$ ions within the heterometallic clusters.[42] The canonical intervalence charge transfer (IVCT) band characteristic of electron transfer between $V^{IV}(d^1)$ centres and $V^{V}(d^0)$ centres was absent suggesting that the cluster possess an isovalent V^{IV} electron configuration. This is analogous to the observations made for the neutral, homoleptic cluster **Ti_2V_4**.[36] This oxidation state distribution is further confirmed by the presence of a weak shoulder around 630 nm, a feature observed in both **Ti_2V_4** and the di-anionic hexavanadium cluster, $[V^{IV}{}_6O_7(OCH_3)_{12}]^{2-}$.[43] Bulk purity of the sample was assessed via elemental analysis (see Experimental Section for details).

Single crystal X-ray diffraction was performed on crystals of **$Ti_2V_4TRIOL^B$** serendipitously grown from the crude reaction mixture, providing an opportunity to unambiguously determine the identity of the product. The refined data reveals the expected heterometallic Lindqvist structure, in which three bridging-methoxide ligands defining a single face of the assembly are replaced by the tridentate $TRIOL^B$ ligand (**Figure 2,** Table S1). Analogous to the previously reported TRIOL-substituted TiPOV-alkoxide clusters, the tridentate ligand is coordinated exclusively at bridging positions located between two vanadium centres.[32] The overall cluster geometry closely resembles that of the homoleptic compound **Ti_2V_4**, with the two titanium centres located *cis* to one another, linked by a bridging-methoxide unit. Both Ti^{IV} centres possess pseudo-octahedral coordination geometries and short Ti–O_m bonds (~1.76 Å) (O_m = oxygen atom of the terminal methoxide ligand). The Ti–O_c (O_c= central μ^6-oxygen atom) bond distance of the cluster is relatively short (~2.133 and ~2.086 Å) compared to the V_t–O_c bond lengths in each cluster (~2.464 Å; V_t= vanadium centre located *trans* to the two titanium centres). As in the case of **Ti_2V_4** and other reported TRIOL-substituted TiPOV-alkoxide clusters, the affinity of the titanium ions for the μ^6-oxo seemingly pulls the oxygen atom out of its central position in the cluster, as evidenced by elongated V_t–O_c bond distances.[32, 36]

Table 1. Electrochemical parameters of complexes **Ti_2V_4**, **$Ti_2V_4TRIOL^{CH3}$**, **$Ti_2V_4TRIOL^B$** and **$Ti_2V_4TRIOL^C$**. Standard potentials (vs. $Ag^+|Ag$) are identified using cyclic voltammetry at 100 mV s^{-1} of 5 mM solutions of each complex with 0.1 M $[^nBu_4N][PF_6]$ supporting electrolyte in MeCN. Values in parentheses indicate ratios of the cathodic and anodic peak heights (i_c/i_a).

	2nd Ti^{III}/Ti^{IV} couple		1st Ti^{III}/Ti^{IV} couple		1st V^{IV}/V^{V} couple		2nd V^{IV}/V^{V} couple	
Complex	$E_{1/2}$ (V)	i_c/i_a	$E_{1/2}$ (V)	i_c/i_a	$E_{1/2}$ (V)	i_c/i_a	$E_{1/2}$ (V)	i_c/i_a
Ti_2V_4	-2.10	1.67	-1.58	1.12	+0.15	1.05	+0.64	0.99
$Ti_2V_4TRIOL^{CH3}$	-2.12	1.53	-1.60	1.15	+0.14	1.01	+0.65	1.14
$Ti_2V_4TRIOL^B$	-2.11	1.33	-1.53	1.14	+0.22	1.1	+0.7	1.25
$Ti_2V_4TRIOL^C$	-2.02	1.25	-1.5	1.01	+0.25	1.2	+0.73	1.3

The redox properties of an analytically pure sample of **Ti_2V_4TRIOL^B** were analyzed via CV. Electrochemical analysis was performed in MeCN with tetrabutylammonium hexafluorophosphate ($[^nBu_4N][PF_6]$) as the supporting electrolyte in order to draw comparisons between the redox profile of the title compound and similar assemblies reported previously by our laboratory. Four quasi-reversible electrochemical events are observed, with half wave potentials analogous to both the homoleptic cluster **Ti_2V_4** and other TRIOL-substituted TiPOV-alkoxide clusters (**Figure 3, Table 1**).[32, 44]

Electronic absorption spectroscopy was used to confirm the oxidation state distribution of transition metal ions in the oxidized and reduced forms of the **Ti_2V_4TRIOL^B**, generated via bulk electrolysis (**Figure 4**).[42, 43] The oxidation processes ($E_{1/2}$ = 0.15, 0.64 V vs. $Ag^{+|0}$ in **Ti_2V_4** are assigned to successive, one-electron vanadium-based processes ($V^{IV} \rightarrow V^V + e^-$), while the two reductive events ($E_{1/2}$ = -1.58, -2.1 V vs. $Ag^{+|0}$ in **Ti_2V_4** are assigned to the reduction processes localized at one of the two titanium ions in the Lindqvist core ($Ti^{IV} + e^- \rightarrow Ti^{III}$). Accordingly, we hypothesized that the two reduction events in the voltammogram of **Ti_2V_4TRIOL^B** ($E_{1/2}$ = −1.53 V, −2.11 V) correspond to sequential Ti^{IV}/Ti^{III} redox couples, whereas the observed series of oxidation events ($E_{1/2}$ = +0.22 V, +0.70 V) are assigned to the V^V/V^{IV} couples.

Spectroelectrochemical characterization of mono-reduced and mono-oxidized forms of **Ti_2V_4TRIOL^B** confirms our assignments of these redox processes. The electronic absorption spectrum of the mono-reduced cluster, **$[Ti_2V_4TRIOL^B]^{1-}$**, possesses a weak absorption around 630 nm (ε = 140 $M^{-1}cm^{-1}$), consistent with a V_4^{IV} electronic configuration. The absorption feature at 422 nm which corresponds to the intervalence charge transfer (IVCT) between V^{IV} and Ti^{IV} ions in reduced in intensity from that of the **Ti_2V_4TRIOL^B**, (ε = 656 $M^{-1}cm^{-1}$ to 625 $M^{-1}cm^{-1}$) consistent with reduction of a single titanium centre. The electronic absorption spectrum of the mono-oxidized form of **Ti_2V_4TRIOL^B** exhibit intense absorption features at 388 nm (ε = 4428 $M^{-1}cm^{-1}$) and around 1000 nm (ε = 478 $M^{-1}cm^{-1}$). It should be noted that this feature is not a discrete peak due to the operable wavelength window of the instrument and the true λ_{max} can be $\geq$ 1000 nm. The transition at lower energies is assigned to an IVCT event between V^{IV} and

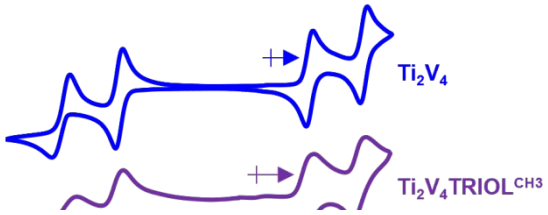

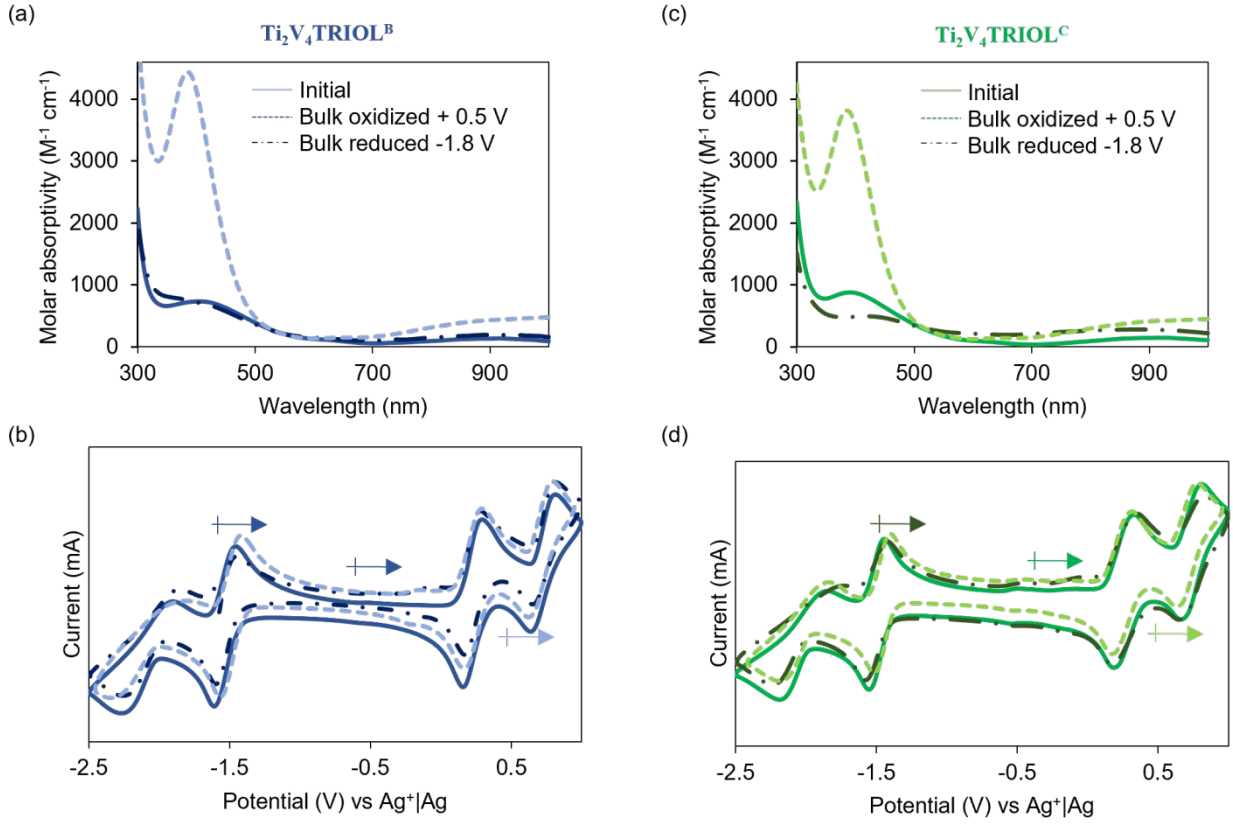

Figure 4. (a) Electronic absorption spectra and (b) cyclic voltammograms of **Ti_2V_4TRIOL^B** demonstrating successful bulk oxidation and reduction. All experiments were performed at room temperature in MeCN with 0.1 M $[^nBu_4N][PF_6]$ as the supporting electrolyte. The analogous data for bulk electrolysis of **Ti_2V_4TRIOL^C** are shown in panels (c) and (d). Note that the CV data in panels (b) and (d) were shifted vertically to overlay the data; the vertical positions of the crossed arrows demarcate zero current flow.

V^V metal centres, consistent with the oxidation event occurring at vanadium. The durability of complex **Ti_2V_4TRIOL^B** across the +1 and -1 charge states was assessed by monitoring the charged solutions using CV at room temperature (Figure S4). Over the course of one week, no evidence of degradation of the charge carrier was noted, indicating that **Ti_2V_4TRIOL^B** is stable across at least a 1.73 V potential range at room temperature. The outer redox events observed in the CV of **Ti_2V_4TRIOL^B** ($E_{1/2}$ = -2.11 V, +0.70 V vs $Ag^{+|0}$) result in the formation of redoxmers that are not stable (see bulk electrolysis experiments in Figure S19); as such we limit battery analysis to the inner electrochemical processes ($E_{1/2}$ = -1.53 V, +0.22 V vs $Ag^{+|0}$).

Next, we targeted the synthesis of a TiPOV-alkoxide cluster bearing a longer-chain alkoxyether functional group, $[Ti_2V_4O_5(OCH_3)_{11}(OCH_2)_3CCH_2OC_2H_4OCH_3]$ (**Ti_2V_4TRIOL^C**). Successful synthesis was accomplished via analogous reaction conditions and work-up to that described for **Ti_2V_4TRIOL^B**. Complex **Ti_2V_4TRIOL^C** was isolated as a viscous brown oil. Characterization of the product via Infrared spectroscopy was used to confirm the formation of the desired Lindqvist species; two absorption bands are observed at ~975 cm^{-1} and ~1020 cm^{-1}, corresponding to $\nu(V{=}O_t)$ (O_t = terminal oxo) and $\nu(O_b\text{-}CH_3)$ (O_b = bridging oxo), with an additional feature at 1125 cm^{-1} assigned to the $\nu(O_t\text{-}CH_3)$ of the terminal alkoxide ligand bound to titanium (Figure S3). Bulk purity of the cluster was assessed via elemental analysis (see Experimental Section for details).

Electrochemical analysis of **Ti_2V_4TRIOL^C** was performed via CV; the resultant voltammogram is similar to that observed for the parent cluster **Ti_2V_4** and complex **Ti_2V_4TRIOL^B** (**Figure 3**). Both bulk electrolysis afforded complete conversion of the cluster assembly to its mono-oxidized and mono-reduced charge-states, respectively (**Figure 4**). Characterization of the oxidized and reduced forms of via electronic absorption spectroscopy revealed analogous changes in the spectroscopic profile to that observed for **Ti_2V_4TRIOL^C.** The spectrum of the oxidized assembly possesses strong transitions at 388 nm (ε = 3805 $M^{-1}cm^{-1}$) and 1000 nm (ε = 453 $M^{-1}cm^{-1}$), consistent with an oxidation localized to the vanadium centres of the TiPOV-alkoxide cluster. In contrast, a sample of **Ti_2V_4TRIOL^C** subjected to reducing potentials indicates that cluster reduction is localized to a titanium centre, as indicated by a reduction in the molar absorptivity of the $V^{IV} \rightarrow Ti^{IV}$ charge transfer event located at 430 nm (ε = 489 $M^{-1}cm^{-1}$). The long-term stability of the resulting oxidized and reduced solutions at room temperature were assessed *via* CV over a span of 7 days. No substantial changes were observed in peak potential or current response for the CVs of the oxidized and reduced solutions, indicating that **Ti_2V_4TRIOL^C** is also stable at room temperature in the one-electron oxidized and reduced states (Figure S4).

Our primary motivation behind the organic functionalization of TiPOV-alkoxide clusters is to improve the solubility of the heterometallic assembly in MeCN for flow battery applications. As such, we measured the solubility of analytically pure samples of **Ti_2V_4TRIOL^B** (Figure S5, Table S2) and **Ti_2V_4TRIOL^C** (Figure S6, Table S3) in MeCN with 0.1 M $[^nBu_4N][PF_6]$. These conditions were selected to mimic the working conditions of our NAqRFB cell. The solubility of **Ti_2V_4TRIOL^B** and **Ti_2V_4TRIOL^C** are measured as 0.32 ± 0.02 M and 0.66 ± 0.02 M, respectively. These values are significantly higher than those reported by our group for **Ti_2V_4** (0.044 ± 0.003 M).[34] The improved solubility of the TiPOVs upon alkoxyether functionalization are consistent with our prior work on organic functionalization of the hexavandate clusters.[31]

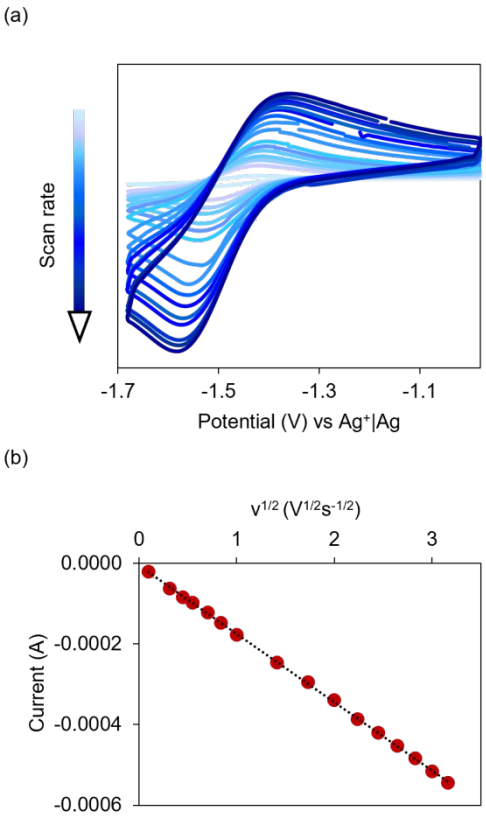

Figure 5. (a) Representative CV measurements of **0/1$^-$** redox couple of 5 mM **Ti_2V_4TRIOL^C** with 0.1 M [nBu4N][PF6] in acetonitrile at scan rates ranging from 10–10 000 mV s^{-1}; (b) Randles–Sevcik analysis of the corresponding data.

Electrokinetic behaviour of alkoxyether-substituted Ti-POVs. Efficient RFB charge carriers must exhibit rapid diffusivity in the electrolyte media.[45] Thus, we evaluated the diffusion coefficients (D_0) of both TRIOL functionalized clusters in MeCN (Figure 5, Figures S7-S9). The redox events associated with one-electron oxidation (**1$^+$/0**) and one-electron reduction (**0/1$^-$**) for both TiPOV alkoxide clusters were isolated and CVs were recorded at scan rates ranging from 10–10000 mV s^{-1} (Figure 5a). The plot of the peak current (i_p) versus the square root of scan rate ($\nu^{1/2}$) exhibits a linear dependence (Figure 5b, Figure S10). This behaviour is characteristic of a diffusion-limited electrochemical process, allowing for the assessment of the D_0 of both TiPOVs using the Randles–Sevcik (R–S) equation.[46] The calculated D_0 values for **1$^+$/0** and **0/1$^-$** of **Ti_2V_4TRIOL^B** are 1.18 ± 2.27 × 10^{-5} cm^2 s^{-1} and 8.92 ± 1.89 × 10^{-6} cm^2 s^{-1}, respectively. Compared to the short-chain ether functionalized cluster, **Ti_2V_4TRIOL^C** exhibits marginally slower diffusion coefficients (**1$^+$/0** = 5.11 ± 0.06 × 10^{-6} cm^2 s^{-1}, **0/1$^-$** = 4.28 ± 0.04 × 10^{-6} cm^2 s^{-1}). The diffusion coefficients measured for

Table 2. Diffusion coefficients and heterogeneous electron transfer rate constants for each redox event in complexes Ti_2V_4, Ti_2V_4TRIOL^B and Ti_2V_4TRIOL^C.

	Ti^{III}/Ti^{IV} couple (**0/1**$^-$)		V^{IV}/V^V couple (**1**$^+$**/0**)	
Complex	D_0 (cm^2 s^{-1})	k_0 (cm s^{-1})	D_0 (cm^2 s^{-1})	k_0 (cm s^{-1})
Ti_2V_4	$9.40 \pm 0.80 \times 10^{-6}$	$1.40 \pm 0.04 \times 10^{-2}$	$1.03 \pm 0.01 \times 10^{-5}$	$7.20 \pm 0.80 \times 10^{-2}$
Ti_2V_4TRIOL^B	$8.92 \pm 1.89 \times 10^{-6}$	$2.97 \pm 0.07 \times 10^{-3}$	$1.18 \pm 2.27 \times 10^{-5}$	$7.55 \pm 0.24 \times 10^{-3}$
Ti_2V_4TRIOL^C	$4.28 \pm 0.04 \times 10^{-6}$	$5.72 \pm 0.15 \times 10^{-3}$	$5.11 \pm 0.06 \times 10^{-6}$	$3.24 \pm 1.11 \times 10^{-3}$

both TiPOV alkoxide clusters are similar to values reported previously for molecular charge carriers.[45, 47]

Next, we evaluated the heterogeneous electron transfer rate constants (k_0) for each relevant redox event in the two assemblies using Nicholson's method.[48] From CVs spanning the scan rate from 10 – 10 000 mV s^{-1}, the difference in peak potential (ΔE_p) was correlated with a dimensionless kinetic parameter (Ψ) (Figures S11-S12).[49] The calculated k_0 for **1**$^+$**/0** and **0/1**$^-$ for the organofunctionalized TiPOV-alkoxide clusters are given in **Table 2**.

According to Marcus's model of electron transfer, the molecular structure of redox active species is expected to affect electron transfer kinetics in both outer- and inner-sphere redox processes.[50] Furthermore, the probability of electron transfer events decreases with increasing distance between the donor and acceptor in the transition state. We thus hypothesized that differences in steric bulk and solvent interactions would yield differences in the kinetics of TiPOV-alkoxide clusters substituted with distinct TRIOL ligands. The electron transfer rate constants for each of the redox events of the homoleptic cluster, **Ti_2V_4**, are reported as **1**$^+$**/0** = $7.20 \pm 0.8 \times 10^{-2}$ cm/s and **0/1**$^-$ = $1.40 \pm 0.04 \times 10^{-2}$ cm/s in MeCN.[34] In comparison, the observed k_0 values for **Ti_2V_4TRIOL^B** are **1**$^+$**/0** = $7.55 \pm 0.24 \times 10^{-3}$ cm/s and **0/1**$^-$ = $2.97 \pm 0.07 \times 10^{-3}$ cm/s. Heterogeneous electron transfer rate constants for **Ti_2V_4TRIOL^C** were determined to be similar to **Ti_2V_4TRIOL^B**, **1**$^+$**/0** = $3.24 \pm 1.11 \times 10^{-3}$ cm/s and **0/1**$^-$ = $5.72 \pm 0.15 \times 10^{-3}$ cm/s.

The observed k_0 values for both TRIOL-substituted TiPOV-alkoxide clusters are reduced by up to 10-fold in comparison to those of **Ti_2V_4**. We attribute this observation to the fact that TRIOL-functionalization decrease the extent of delocalization within the hexametalate core. This suppression of electronic communication across the cluster core manifests as slower rates of electron transfer to and from the cluster assembly. We note that the suppression in rate of electron transfer is more significant for the oxidative process (**1**$^+$**/0**); this observation is consistent with the fact that the TRIOL ligand is attached to the vanadium atoms. Accordingly, redox processes occurring at vanadium centres, like the oxidation reactions in both **Ti_2V_4TRIOL^B** and **Ti_2V_4TRIOL^C** are more substantially affected than rates of Ti-based reduction processes. While the rates of electron transfer are significantly slower for complexes **Ti_2V_4TRIOL^B** and **Ti_2V_4TRIOL^C** as compared to **Ti_2V_4**, it should be noted that these values of heterogeneous rate constants remain high enough to facilitate flow battery operation that is not fundamentally limited by kinetic overpotentials.[47]

Extended charge-discharge cycling. The solubility of the TRIOL functionalized TiPOV-alkoxide clusters, coupled with fast electron transfer kinetics, suggest that these heterometallic complexes can serve as charge carriers in symmetric RFBs, capable of transferring one electron at each electrode. As such, we transitioned from fundamental electrochemical studies to proof-of-concept analyses through static H-cell charge–discharge cycling experiments. Using the expression derived by Sanford and Thompson for calculating the theoretical energy density of a charge carrier (Eqn 3) we can evaluate the theoretical volumetric energy density for each cluster:[51]

$$E = 0.5 \times n \times V_{cell} \times C_{active} \times F \qquad (3)$$

where E is the volumetric energy density, n is the number of electrons transferred, V_{cell} is the average cell voltage, C_{active} is the concentration of active species, and F is Faraday's constant. A V_{cell} of 1.73 V and a solubility of 0.32 M yields an energy density of 27 kJ L^{-1} for **Ti_2V_4TRIOL^B**, which represents a 600 % improvement over that of **Ti_2V_4**. In contrast, a solubility of 0.66 M for **Ti_2V_4TRIOL^C** results in a theoretical energy density of 55 kJ L^{-1}. This value is about 14-fold greater than that obtained for the homoleptic precursor (C_{active} = 0.044 M, V_{cell} = 1.73 V).

The improved theoretical energies densities of **Ti_2V_4TRIOL^B** and **Ti_2V_4TRIOL^C** motivated preliminary investigations into battery cycling experiments through static charge-discharge experiments. Cycling experiments were performed with 5 mM solution of the cluster in MeCN with 0.1 M [^{n}Bu$_4$][PF$_6$] supporting electrolyte in an H-cell. To minimize cell resistance, posolyte and negolyte chambers were separated by a glass frit. We adopted a galvanostatic–potentiostatic sequential cycling method initially reported by Goulet and Aziz,[41] and adapted for TiPOV-alkoxide clusters by our research team.[34] A charging current of 0.2 mA until the potential reached 1.9 V, followed by holding the potential at 1.9 V until the current dropped to 0.02 mA. Similarly, a discharging current of 0.2 mA was applied until a cut off potential of 1.4 V was reached, with a potentiostatic discharge at 1.4 V until the current reached a value of 0.02 mA. **Figure 6a** depicts the first 5 cycles observed during the battery cycling experiment of **Ti_2V_4TRIOL^B** (Full cycling data is provided in Figure S13). Coulombic efficiencies were maintained at 98% over 10 cycles (Figure S14). The rates of capacity loss for both

the charge and discharge cycles are depicted in **Figure 6d**. We observe a 62% capacity loss after 10 cycles. While this degradation is significant, the system reflects greater durability than other electrolyte systems reported in non-aqueous conditions. For example, while Clegg et al. report a 74% capacity fade rate for the $V(acac)_3$ system, Savinell and co-workers have documented 80% capacity fade of the same system after 10 cycles.[52, 53] We hypothesized that the observed reduction in cell capacity results from chemical reactions to deactivate the redox couple in either or both reaction chambers during battery cycling.

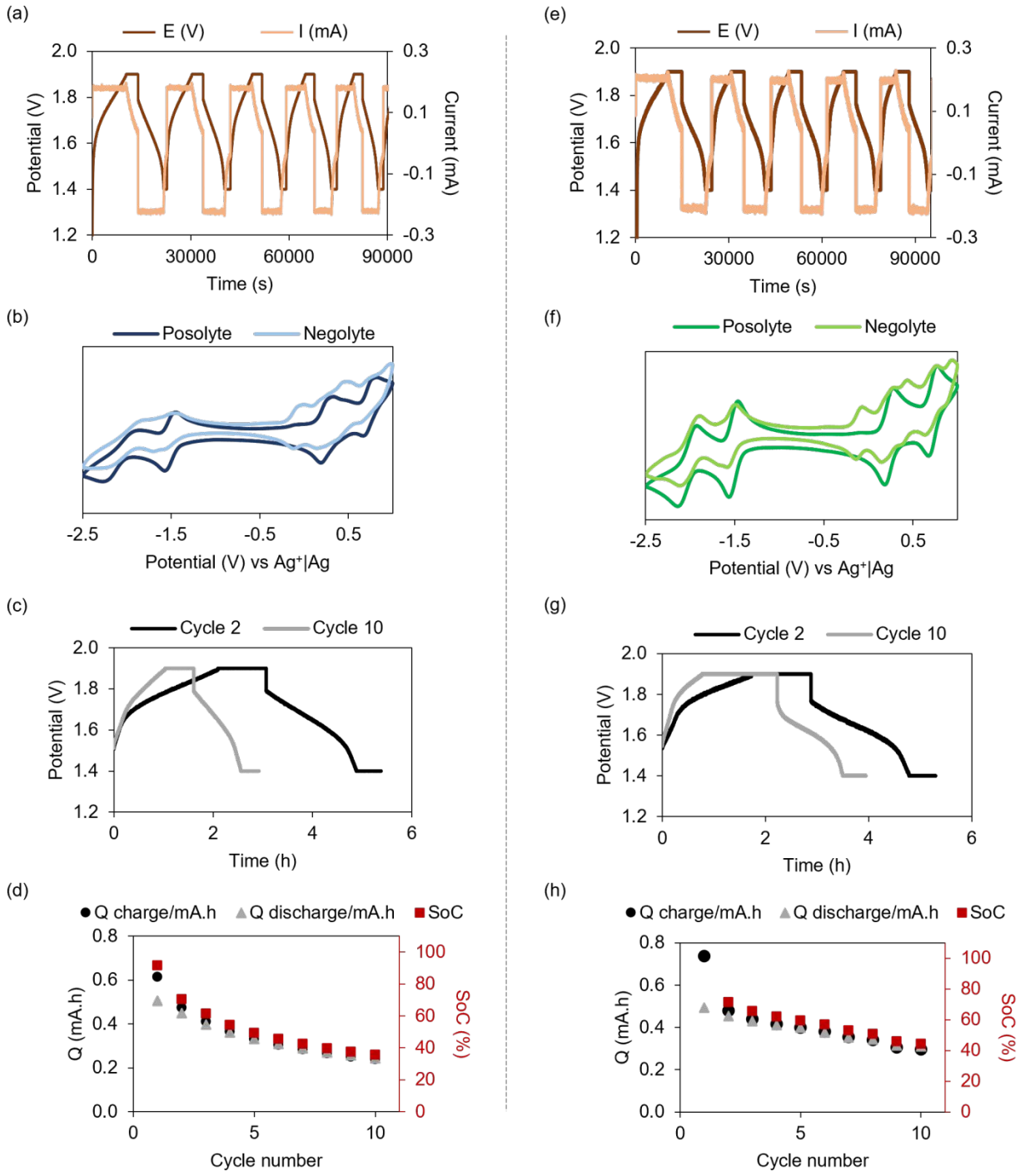

Figure 6. (a) Voltage trace of cycles 1–5 in charge–discharge cycling of $Ti_2V_4TRIOL^B$ (b) Cyclic voltammograms of solutions after charge–discharge cycling (c) Comparison of cycles 2 and 10 from the battery cycling experiment (d) Capacity fade over 10 cycles (black circles represent charging capacity; grey triangles represent discharging capacity; red squares represent percent state of charge (SoC) of the battery) (e)–(h) show similar characterizations for charge–discharge cycling of $Ti_2V_4TRIOL^C$.

Post cycling analysis by CV (**Figure 6b**) demonstrates the positive electrolyte undergoes minimal changes under these cycling conditions. However, partial decomposition of the negative electrolyte (i.e., the electrolyte based on the **0/1**$^-$ charge states) was observed, suggesting that the reduced form of the cluster is less stable. New features emerge in the CV of the negative electrolyte after cycling, which correspond to the electrochemical signature of the mono-titanium derivative of the POV-alkoxide cluster, $[TiV_5O_6(OCH_3)_{13}]^{1-}$ (**TiV_5^{1-}**) as has been previously reported by our research team (Figure S20).[54] We note that the synthetic conditions prescribed for the formation of **TiV_5^{1-}** require additional reductant, suggesting that formation of the mono-titanium derivative of the cluster is favoured over the neutral **Ti_2V_4** complex under reducing conditions. As such,

we pose that cluster rearrangement in the negolyte chamber is facilitated by the highly reducing conditions of our cycling experiment.[32, 36]

A thorough understanding of the prevalent decay mechanisms in RFBs, such as electrode passivation, crossover, electrolyte side reactions, and self-decomposition of the charge carrier, can aid in designing suitable analytical methods to probe sources of capacity fade.[41, 55] To further validate the observed capacity fade due to the instability of the cluster in its reduced charge state, we cycled volumetrically unbalanced compositionally symmetric cells, following methods developed by Aziz and co-workers.[41] The volume of the posolyte was kept at 5 mL, whereas the negolyte was used in excess quantities (10 mL). As depicted in Figure S15, under the same experimental (dis)charging protocol, the overall rate of capacity fade was similar, and the average coulombic efficiency was notably reduced, compared to the case of a balanced configuration. However, less fractional degradation (20% formation of $\mathbf{TiV_5^{1-}}$ as compared to 58 % in previous cases) of the negative electrolyte is observed. We believe that this is due to the fact that more cluster is present in the negolyte chamber, reducing the state of charge for the reductive cycling required. Similarly, we observe improved capacity retention on increasing the concentration of the negolyte (Figure S17). In the case of these battery cycling configurations, the capacity drops by only 40% for $\mathbf{Ti_2V_4TRIOL^B}$ after 10 cycles. This value of battery capacity degradation rate is less than that obtained using other charge-discharge techniques (*vide supra* 62% for equimolar and volumetrically balanced cell; 58% for equimolar, volumetrically imbalanced cell).

We also carried out galvanostatic polarity-reversal experiments of $\mathbf{Ti_2V_4TRIOL^B}$ to test whether it is possible to reduce degradation even further (Figure S16). Our hypothesis behind reversing the polarity of the electrochemical cell was to distribute the degradation over both electrolyte sides so that we can harness more charge-discharge cycles without significant decomposition of the negative electrolyte.[6] Indeed, our results demonstrate that the practical capacity remains higher (20% average capacity fade over 10 cycles as compared to 62% with prior techniques) when degradation is distributed over both of the symmetric battery electrolytes. We observe the least amount of $\mathbf{TiV_5^{1-}}$ formation (13%) using this methodology. It should be noted that the observed absolute capacity is lower in this case due to the purely galvanostatic mode of cycling. These results further support a purely chemical mechanism for the observed capacity fade.

Similar charge-discharge experiments were conducted for $\mathbf{Ti_2V_4TRIOL^C}$. Analogous to $\mathbf{Ti_2V_4TRIOL^B}$, we observe no decomposition of the positive electrolyte, while the negative electrolyte partially degrades to yield the mono-titanium cluster (**Figure 6(f)**). No additional plateaus are detected during the experiment and coulombic efficiencies are maintained at 90% over 10 cycles (Figures S14-S15). In contrast to the short-chain derivative, $\mathbf{Ti_2V_4TRIOL^C}$ reaches the voltage limit driving the programmatic transition to potentiostatic charging earlier during the charge cycle (**Figure 6(e)**). We attribute this behaviour to the slower diffusion coefficients of $\mathbf{Ti_2V_4TRIOL^C}$ which increases polarization under galvanostatic conditions. This observation is consistent with our previously reported study on $\mathbf{Ti_2V_4}$, where slower diffusivity of the charge carrier in mixed or more viscous solvents resulted in predominantly potentiostatic mode of charge-discharge.[34] Since the capacity observed during galvanostatic cycling with potential limits is directly related to the polarization resistance of the cell,[41] we conclude that $\mathbf{Ti_2V_4TRIOL^C}$ is more susceptible to voltage efficiency losses as compared to $\mathbf{Ti_2V_4TRIOL^B}$ in pure galvanostatic mode of cycling. However, as pointed out by Goulet and Aziz in their seminal report, potentiostatic cycling with steady state current cut-offs enables to access nearly 100% of the theoretical capacity, thereby minimizing the impact of polarization resistance at the expense of longer charge-discharge cycles. Hence, the results presented here represent a rigorous preliminary assessment of the cyclability of these TiPOV-alkoxide clusters, and we speculate that cycle-life durability would be greater under galvanostatic operation in a flow cell.

The degradation of $\mathbf{Ti_2V_4TRIOL^B}$ and $\mathbf{Ti_2V_4TRIOL^C}$ during cycling experiments is surprising, given the stability of the oxidized and reduced forms of the TiPOV-alkoxide charge carriers over 7 days following bulk electrolysis (*vide supra,* Figure S4). In considering a justification for this observation, we note that our stability analysis was conducted with samples stored at room temperature. RFBs generate heat when consuming electric power in their working state.[57] As such, activation, ohmic and concentration losses can manifest during battery cycling as the reaction kinetics and transport properties of the electrolyte are functions of temperature.[58, 59] These losses can affect the battery performance metrics (such as state-of-charge, SOC) and can also result in the degradation of the active material. To evaluate whether the degradation in the TRIOL systems during charge-discharge is a result of heat generation, we heated the bulk oxidized and reduced samples of $\mathbf{Ti_2V_4TRIOL^B}$ at 30^{o}C and stirred them for 7 days to simulate the speculated heat generation during battery cycling. Our results demonstrate degradation of both posolyte and negolyte after 7 days (Figure S18). These conditions are expected to be more extreme than the actual experiment and explain the deterioration of the posolyte solution contrary to that observed in the charge-discharge experiment. Hence, we hypothesize that the observed degradation of the negolyte for the TRIOL-capped TiPOVs during battery cycling is a result of the thermal effects that arise during the working of the battery. We note that we cannot rule out over-oxidation or over-reduction of the cluster to the doubly charged species under the employed cycling conditions. This fact may further contribute to the instability of the system. Hence, the chemical stability of the cluster would need to be improved across all charge states to further assess the implications of alkoxyether functionalization of TiPOVs in flow cell applications.

Conclusions

Understanding the physical and electrochemical implications of bridging alkoxide ligands appended with ether functional

groups is essential for the future of POV-based charge carriers, as these moieties are established to yield improved solubility in MeCN.[31, 51, 60] In this work, we demonstrate that synthetic modifications can impart substantial improvement to the solubility TiPOV-alkoxide assemblies. The enhancement in solubility and cell voltage for **Ti_2V_4TRIOL^B** and **Ti_2V_4TRIOL^C** results in significant improvements of the *theoretical* energy storage capabilities of these heterometallic clusters over their hexavanadate congeners; however, the experimental cycling data demonstrates decomposition of the negolyte. The resulting TRIOL-substituted clusters exhibit heterogeneous rate constants of electron transfer that are an order of magnitude slower than those observed for **Ti_2V_4**. We attribute this behaviour to decreased delocalization in the hexametalate core upon alkoxyether functionalization, but the effect is not large enough to preclude viability of this charge carrier in functional NAqRFBs.

Additional studies probing the charge-discharge behaviour of the TRIOL functionalized titanium-substituted POV-alkoxide clusters reveal distinct cycling response. While **Ti_2V_4TRIOL^B** exhibits primarily galvanostatic mode of (dis)charge, **Ti_2V_4TRIOL^C** demonstrates predominantly potentiostatic cycling and hence longer charging cycles. We ascribe this behaviour to the difference in the diffusion coefficients of the two assemblies that leads to polarization resistance in the electrochemical cell. Charge–discharge experiments of both TRIOL-substituted TiPOV-alkoxide clusters yield decomposition of the negolyte. Probing the decomposition of these complexes using temperature dependent bulk-electrolysis experiments indicate that the observed degradation of the negative electrolyte is likely a result of the thermal effects that arise during the working of the battery. Ongoing investigations in our laboratory are focused on the impact of temperature on the kinetics of electron transfer and degradation for further exploration in the development of efficient RFBs.

Author Contributions

M.D., D.M.M.M.D, and E.M.M. conceived and planned the experiments. M.D., D.M.M.M.D., J.D.M., D.N.K., and M.C. performed all synthetic and electrochemical experiments and interpreted results. W.W.B. collected and refined data to determine the crystal structure of **Ti_2V_4TRIOL^B**. The manuscript was composed by M.D. and E.M.M.; all authors have given approval to the final version of the manuscript.

Conflicts of interest

J.R.M. is currently an advisory board member and may in the future gain equity interest in a company that develops technologies for redox flow batteries.

Acknowledgements

The authors acknowledge Prof. Timothy Cook (University at Buffalo) for helpful conversations during this project. This research was funded by the National Science Foundation, Division of Chemical, Bioengineering, Environmental, and Transport Systems Program (Awards 2015749 and 2015859).

Notes and references

1. C. P. de Leon, A. Frias-Ferrer, J. Gonzalez-Garcia, D. A. Szanto and F. C. Walsh, *Journal of Power Sources*, 2006, **160**, 716-732.
2. W. Wang, Q. T. Luo, B. Li, X. L. Wei, L. Y. Li and Z. G. Yang, *Advanced Functional Materials*, 2013, **23**, 970-986.
3. K. Gong, Q. R. Fang, S. Gu, S. F. Y. Li and Y. S. Yan, *Energy & Environmental Science*, 2015, **8**, 3515-3530.
4. T. V. Sawant, C. S. Yim, T. J. Henry, D. M. Miller and J. R. McKone, *Joule*, 2021, **5**, 360-378.
5. M. Park, J. Ryu, W. Wang and J. Cho, *Nature Reviews Materials*, 2017, **2**.
6. R. A. Potash, J. R. McKone, S. Conte and H. D. Abruna, *Journal of the Electrochemical Society*, 2016, **163**, A338-A344.
7. G. S. Nambafu, *Electrochemistry Communications*, 2021, **127**.
8. H. Wang, S. Hamanaka, Y. Nishimoto, S. Irle, T. Yokoyama, H. Yoshikawa and K. Awaga, *Journal of the American Chemical Society*, 2012, **134**, 4918-4924.
9. Y. Z. Liu, G. H. Wen, J. C. Liang, S. S. Bao, J. Wei, H. Z. Wang, P. B. Zhang, M. F. Zhu, Q. Q. Jia, J. Ma, L. M. Zheng and Z. Jin, *ACS Energy Letters*, 2023, **8**, 387-397.
10. J. Friedl, M. V. Holland-Cunz, F. Cording, F. L. Pfanschilling, C. Wills, W. McFarlane, B. Schricker, R. Fleck, H. Wolfschmidt and U. Stimming, *Energy & Environmental Science*, 2018, **11**, 3010-3018.
11. F. Ai, Z. Y. Wang, N. C. Lai, Q. L. Zou, Z. J. Liang and Y. C. Lu, *Nature Energy*, 2022, **7**, 417-426.
12. W. Yan, C. Wang, J. Tian, G. Zhu, L. Ma, Y. Wang, R. Chen, Y. Hu, L. Wang, T. Chen, J. Ma and Z. Jin, *Nat Commun*, 2019, **10**, 2513-2524.
13. J. Wei, P. B. Zhang, Y. Z. Liu, J. C. Liang, Y. R. Xia, A. Y. Tao, K. Q. Zhang, Z. X. Tie and Z. Jin, *Acs Energy Letters*, 2022, **7**, 862-870.
14. H. D. Pratt, N. S. Hudak, X. K. Fang and T. M. Anderson, *Journal of Power Sources*, 2013, **236**, 259-264.
15. H. D. Pratt, W. R. Pratt, X. K. Fang, N. S. Hudak and T. M. Anderson, *Electrochimica Acta*, 2014, **138**, 210-214.
16. A. Proust, R. Thouvenot and P. Gouzerh, *Chemical Communications*, 2008, DOI: 10.1039/b715502f, 1837-1852.
17. P. Gouzerh and A. Proust, *Chemical Reviews*, 1998, **98**, 77-111.
18. C. L. Peake, A. J. Kibler, G. N. Newton and D. A. Walsh, *Acs Applied Energy Materials*, 2021, **4**, 8765-8773.
19. J. M. Cameron, G. Guillemot, T. Galambos, S. S. Amin, E. Hampson, K. M. Haidaraly, G. N. Newton and G. Izzet, *Chemical Society Reviews*, 2022, **51**, 293-328.
20. D. L. Long, R. Tsunashima and L. Cronin, *Angewandte Chemie-International Edition*, 2010, **49**, 1736-1758.
21. L. Cronin and A. Muller, *Chemical Society Reviews*, 2012, **41**, 7333-7334.
22. S. Chakraborty, B. E. Petel, E. Schreiber and E. M. Matson, *Nanoscale Advances*, 2021, **3**, 1293-1318.

23. Y. Hayashi, *Coordination Chemistry Reviews*, 2011, **255**, 2270-2280.
24. K. Y. Monakhov, W. Bensch and P. Kogerler, *Chemical Society Reviews*, 2015, **44**, 8443-8483.
25. Q. Chen, D. P. Goshorn, C. P. Scholes, X. L. Tan and J. Zubieta, *Journal of the American Chemical Society*, 1992, **114**, 4667-4681.
26. M. I. Khan, Q. Chen, J. Zubieta and D. P. Goshorn, *Inorganic Chemistry*, 1992, **31**, 1556-1558.
27. C. Qin and J. Zubieta, *Inorganic Chemistry*, 1990, **29**, 1456-1458.
28. J. W. Han and C. L. Hill, *Journal of the American Chemical Society*, 2007, **129**, 15094-15095.
29. C. Allain, S. Favette, L. M. Chamoreau, J. Vaissermann, L. Ruhlmann and B. Hasenknopf, *European Journal of Inorganic Chemistry*, 2008, DOI: 10.1002/ejic.200701331, 3433-3441.
30. X. L. Hu, Z. C. Xiao, B. Huang, X. K. Hu, M. Cheng, X. J. Lin, P. F. Wu and Y. G. Wei, *Dalton Transactions*, 2017, **46**, 8505-8513.
31. L. E. VanGelder, B. E. Petel, O. Nachtigall, G. Martinez, W. W. Brennessel and E. M. Matson, *Chemsuschem*, 2018, **11**, 4139-4149.
32. L. E. VanGelder, W. W. Brennessel and E. M. Matson, *Polyhedron*, 2019, **167**, 119-126.
33. B. E. Schurr, O. Nachtigall, L. E. VanGelder, J. Drappeau, W. W. Brennessel and E. M. Matson, *Journal of Coordination Chemistry*, 2019, **72**, 1267-1286.
34. M. Dagar, M. Corr, T. R. Cook, J. R. McKone and E. M. Matson, *Journal of Materials Chemistry A*, 2023, **11**, 13729-13741.
35. C. Daniel and H. Hartl, *Journal of the American Chemical Society*, 2005, **127**, 13978-13987.
36. L. E. Vangelder, P. L. Forrestel, W. W. Brennessel and E. M. Matson, *Chemical Communications*, 2018, **54**, 6839-6842.
37. T. J. Dunn, W. L. Neumann, M. M. Rogic and S. R. Woulfe, *Journal of Organic Chemistry*, 1990, **55**, 6368-6373.
38. G. R. Fulmer, A. J. M. Miller, N. H. Sherden, H. E. Gottlieb, A. Nudelman, B. M. Stoltz, J. E. Bercaw and K. I. Goldberg, *Organometallics*, 2010, **29**, 2176-2179.
39. I. A. Gorodetskaya, T. L. Choi and R. H. Grubbs, *Journal of the American Chemical Society*, 2007, **129**, 12672-12673.
40. J. C. Myland and K. B. Oldham, *Analytical Chemistry*, 2000, **72**, 3972-3980.
41. M. A. Goulet and M. J. Aziz, *Journal of the Electrochemical Society*, 2018, **165**, A1466-A1477.
42. L. E. Vangelder, M. Kosswattaarachchi, A., P. L. Forrestel, T. R. Cook and E. M. Matson, *Chemical Science*, 2018, **9**, 1692-1699.
43. C. Daniel and H. Hartl, *Journal of the American Chemical Society*, 2009, **131**, 5101-5114.
44. L. E. Vangelder and M. Matson, Ellen, *Journal of Materials Chemistry A*, 2018, **6**, 13874-13882.
45. B. Yang, L. Hoober-Burkhardt, F. Wang, G. K. S. Prakash and S. R. Narayanan, *Journal of the Electrochemical Society*, 2014, **161**, A1371-A1380.
46. Q. H. Liu, A. E. S. Sleightholme, A. A. Shinkle, Y. D. Li and L. T. Thompson, *Electrochemistry Communications*, 2009, **11**, 2312-2315.
47. A. Z. Weber, M. M. Mench, J. P. Meyers, P. N. Ross, J. T. Gostick and Q. H. Liu, *Journal of Applied Electrochemistry*, 2011, **41**, 1137-1164.
48. R. S. Nicholson, *Analytical Chemistry*, 1965, **37**, 1351-1355.
49. T. V. Sawant and J. R. McKone, *Journal of Physical Chemistry C*, 2019, **123**, 144-152.
50. R. A. Marcus, *Journal of Chemical Physics*, 1965, **43**, 679-701.
51. J. A. Suttil, J. F. Kucharyson, I. L. Escalante-Garcia, P. J. Cabrera, B. R. James, R. F. Savinell, M. S. Sanford and L. T. Thompson, *Journal of Materials Chemistry A*, 2015, **3**, 7929-7938.
52. C. Clegg and I. G. Hill, *Journal of the Electrochemical Society*, 2020, **167**, 120510-120520.
53. I. L. Escalante-Garcia, J. S. Wainright, L. T. Thompson and R. F. Savinell, *Journal of the Electrochemical Society*, 2015, **162**, A363-A372.
54. L. E. VanGelder, W. W. Brennessel and E. M. Matson, *Dalton Transactions*, 2018, **47**, 3698-3704.
55. Y. X. Yao, J. F. Lei, Y. Shi, F. Ai and Y. C. Lu, *Nature Energy*, 2021, **6**, 582-588.
56. N. H. Mitchell and N. Elgrishi, *Journal of Physical Chemistry C*, 2023, **127**, 10938-10946.
57. S. L. Huang, C. P. Li, C. C. Chang, C. C. Tseng, M. W. Wang and M. L. Chen, *Energies*, 2020, **13**, 6717-6736.
58. D. E. Eapen, S. R. Choudhury and R. Rengaswamy, *Applied Surface Science*, 2019, **474**, 262-268.
59. J. Y. Ren, Y. J. Li, Z. Y. Wang, J. Sun, Q. L. Yue, X. Z. Fan and T. S. Zhao, *International Journal of Heat and Mass Transfer*, 2023, **203**, 123818-123838.
60. J. D. Milshtein, A. P. Kaur, M. D. Casselman, J. A. Kowalski, S. Modekrutti, P. L. Zhang, N. H. Attanayake, C. F. Elliott, S. R. Parkin, C. Risko, F. R. Brushett and S. A. Odom, *Energy & Environmental Science*, 2016, **9**, 3531-3543.